Chapter

Impact of Dopants on the Electrical and Optical Properties of Hydroxyapatite

Kumaravelu Thanigai Arul, Jayapalan Ramana Ramya and Subbaraya Narayana Kalkura

Abstract

This chapter deals with the effect of alternating electrical current on hydroxyapatite [HAp, $Ca_{10}(PO_4)_6(OH)_2$] and doped HAp along with their optical response and the processes involved. The dielectric constant, permittivity and ac conductivity were analyzed to have an insight into the surface charge polarization phenomenon. Further, the magnitude and the polarity of the surface charges, microstructure, and phases also play significant role in the cell proliferation and growth on the implants. Besides, the mechanism behind the electrical properties and the healing of bone fracture are discussed. The influence of various dopants on the optical properties of HAp viz., absorbance, transmission, band gaps and defects energy levels are analyzed along with the photoluminescence and excitation independent emission. In the future outlook, the analysis of effect of doping is summarized and its impact on the next generation biomaterials are elucidated.

Keywords: doped hydroxyapatite, electrical, optical, luminescence

1. Introduction

Hydroxyapatite (HAp) is one of the phases of calcium phosphate having excellent biological properties. Human bone contains 75% of inorganic materials (HAp) and remaining organic contents (predominantly collagen) and water. The HAp is analogous to the inorganic compositions of bone. The drawbacks of HAp to be used as an implant (bone and dental replacement material) are its weak mechanical strength, resorbability and to an extent this could be overcome by doping with metal ions. However, there were no adequate new bone formation between living bone and the implants due to the slow osteoconductivity [1]. Even variations in shape, roughness of the implants did not enhance osteoconduction [2]. Some other routes say tissue engineering, even growth factors [bone morphogenic protein (BMP)] [3] etc., also possess some treatment issues. Further, these parameters could not improve the osteoconduction. So, the application of the electric field on the HAp nanoparticles to induce strongly or weakly oriented dipoles, depending on the polarization of the dopants and band gap of the HAp nanoparticles to improve its biocompatibility. Besides, the dopants modify the ionic and space charge polarizations which vary with the ionic size of the dopants.

Recently, many studies have been reported on the electrical properties of HAp/doped HAp. Das and Pamu suggested that HAp could be a suitable candidate

for biosensing and micro-electromechanical system applications [4]. The ferroelectric properties of graphene-doped HAp samples were studied by Hendi and Yakuphanoglu [5]. Iron-doped calcium phosphate demonstrated hyperthermia (42°C) within 4 minutes [6]. Study on various metals ions (iron, manganese, and cobalt ions)-doped HAp revealed an increase in the ac conductivity. Further, the annealed iron-doped HAp revealed ferromagnetism, whereas the manganese and cobalt ions doped samples exhibited super-paramagnetic property [7]. The dielectric properties of the chromium-doped HAp were also studied [8]. Various anions such as nitrate, acetate, chloride, and egg shell precursors have been used to prepare HAp particles and their corresponding dielectric constant were 9.96, 13.22, 9.92, and 10.86 at 5 MHz [9]. Porous HAp was prepared from *Pila globosa* shells which possessed high dielectric constant with low dielectric loss [10]. HAp-barium titanate (BT) composite scaffolds having improved electric, compressive strength, toughness, density, and hardness were developed using cold isostatic pressing and sintering by Tavangar et al. [11]. Bismuth ions (10, 30 and 50 wt%) were substituted in the HAp matrix by the conventional solid-state reaction at 1300°C and their ac conductivity was reduced with an increase in Bi content [12]. Space charge and dipolar polarization were the dominant polarization mechanisms in $Na_{0.5}K_{0.5}NbO_3$ (NKN)-HAp as reported by Verma et al. [13]. La, Ba, Fe, and Zn ions doped HAp synthesized by sol-gel route displayed a space charge polarization at low frequency with negative temperature coefficient of resistance [14]. Different contents (e.g., 0, 1, 3, 6, 19, 12, and 15% [wt.]) of gallium ion-doped HAp by microwave-assisted sol-gel technique, illustrated a higher inhibition of bacteria and fungi. Further, gallium ions influence the dielectric properties of HAp [15]. Dielectric properties of chlorinated ethylene propylene diene monomer/hydroxyapatite nanocomposites were robustly distorted at lower frequencies whereas above 103 Hz, it was frequency independent [16]. Horiuchi et al. reported that the polycrystalline HAp possesses conductive grains and insulating grain boundaries further, interfacial polarization was confirmed to be an electret [17]. In the case of chitosan/HAp composite, the concentration of chitosan plays a predominant role in regulating its hardness, conductivity and dielectric constant [18]. HAp particles were permanently polarized by both electric potential (500 V direct current) and thermal treatment (at 1000°C) leading to the high adsorption of inorganic bioadsorbates compared to the as prepared HAp [19]. Electric field assisted sintering such as spark plasma sintering (SPS) and flash sintering (FS) performed on HAp revealed nanovoids within HA grains. Further, in situ TEM heating produced nanovoids which remained stable up to 900°C and were not present at 1100°C [20]. Using sol-gel route, yttrium and strontium co-substituted nano-hydroxyapatite was prepared with a minor phase of β tricalcium phosphate, however the ac conductivity was enhanced with an increase in frequency [21]. Tungsten-doped hydroxyapatite (W-HAp) nanoparticles were prepared by chemical precipitation followed by thermal treatment (800, 1000 and 1200°C) leading to an enhancement in the mechanical strength, Young's modulus and dielectric constant [22]. The synthesis routes, concentration of doping, and doping characteristics affect the behavior of dielectrics as well as other correlated properties such as mechanical and biocompatibility. In the case of doping of semiconductors, the dielectric properties are robustly influenced due to the presence of holes and electrons. When the electric field is applied, the polarization varied in the matrix owing to the occurrence of both holes and electrons. The physical (pressure), chemical (electronic), and thermal treatment significantly alter the properties of HAp leading to the creation of porous, dense and bonded matrix. When electric field is applied to such systems, the electronic polarization, oxygen vacancies, dipole displacement, and atomic orientation are interrelated which alter the

permittivity and ac conductivity of HAp. In the case of polymer/HAp composites, the dielectric behavior is distinct due to the presence of carbon and hydrogen chains and the type of bonding. On annealing, the dielectric response of the composites changes significantly due to the formation of voids and porous structures.

Yamashita et al. reported the chemical effects of the electrically polarized HAp in simulated body fluid [23] and in addition enhanced the *in vitro* bioactivity and *in vivo* osteoconductivity [24, 25]. Similarly, the bioactivity of HAp has been improved by doping of metal ions viz., iron [26, 27], silver [28, 29], magnesium [30, 31], strontium [32, 33], etc., in HAp. Co-dopants like magnesium-silver ions [34], iron-zinc [35], etc., have also been used for augmenting physical and biological properties. Electrical and dielectric properties of HAp are crucial for understanding the dipole polarization and surface charge. Depending on the radius of metal ions, substitution or doping takes place in the matrix of HAp which in turn alters the local dielectric polarization leading to micro and macro polarization. Further, these types of polarization modify the surface charges to either positive or negative. In the case of co/tri doping, the basis of lattice has higher atomic and electronic polarization which alter local bonding of the atoms. When electromagnetic field is applied to the co-doped lattice, the wave dispersion is modified when compared to the pristine dielectric material. The ex situ electromagnetic fields enhance the bone fracture healing and bone mineralization [36]. Bowen et al. reported that an enhancement in the barium titanate incorporation in HAp lattice increases the permittivity and ac conductivity [37]. Nakamura et al. revealed the migration of protons along the columnar structure of HAp under electric field at high temperature [38]. Enhanced bone growth was noticed on the negatively charged surface whereas it was reduced on positively charged surface [39]. Osteogenesis was promoted in the dog's jawbones using HA-$BaTiO_3$ composites without any change in phase [40]. Nakamura et al. augmented the osteoconduction of the canine bone owing to the bioactive HAp surface as well as accelerated surface charge by electrical polarization [41]. In the lattice of HAp, the hydroxyl atoms were projected along c-axis and charges are modified on application of the electric field and with an increase in temperature. The projection of hydroxyl groups alters to either abundant negative or positive charge that would aid the cell growth and cell proliferation.

The interaction of light with the HAp nanoparticles is another interesting phenomenon, though an insulating material, the presence of phosphate ions aids the emission of photons of different wavelengths. Addition of metal ions in the lattice of HAp tunes the defect energy levels and alters the chemical potential. The dopants can affect the optical and photoluminescence (PL) of HAp. These properties depend on the absorption, transmission, and band gap as well. Further, these properties favor the use of the HAp nanostructure for bio-imaging and biosensing applications. The doped HAp facilitates the trapping of photons at defect sites or ease transmission which enables them for opto-electronic device applications. Popa and Ciobanu reported the enhanced PL by the cerium ions doped HAp without any structural change [42]. The band gap of erbium-doped HAp was reduced displaying red and green emissions [43]. The various emissions were possible due to the formation of defect energy levels coupled with the HAp energy levels which alters the rate of recombination of electron and hole pairs. Further, the doping concentration varies the active centers of recombination. Feng et al. reported that the Eu^{3+}/Gd^{3+}dual-doped HAp nanorods show enhanced PL with a sustained ibuprofen (IBU) release. Further, the nanorods were injected into mice and demonstrated that these nanorods could be used for *in vivo* imaging [44]. Europium-doped HAp revealed high photoluminescence intensity at 900°C due to the migration of europium from Ca1 to Ca2 site [45]. Fluorescent europium-doped HAp nanowires were prepared by hydrothermal technique and in situ dispersion of them for dental applications [46]. Chang et al.

reported dual emission from nitrogen-doped carbon dots (N-CDs)/HAp:europium, gadolinium composite due to aggregation of N-CDs [47]. The nanostructures either one or zero dimensions significantly affect the electronic motion forming many energy levels due to the quantum confinement effect. Moreover, the optical properties of HAp vary on doping of quantum dots, nanowires, etc. When light is shone on the materials, various local emissions occurred that would be absorbed in the matrix subsequently leading to the partial emission of photons. In the case of cerium-doped HAp, the luminescence quenching occurred between the nearest cerium ions in the matrix as reported by Kolesnikov et al. [48]. Various fluoridated HAp doped with Eu^{3+} ion nanoparticles were prepared by hydrothermal technique and the fluorine ions could influence the crystal field environment for luminescence conversion [49]. Reddy et al. observed a strong green emission from Ni^{2+}-doped Ca-Li HAp (CLHA) [50]. Erbium-ytterbium-molybdenum tri-doped HA/β-TCP phosphor was synthesized using solid-state reaction by Van et al. They demonstrated 650 times higher green emission in the presence of molybdenum [51]. In the case of tri-doped HAp, each dopant generates its energy levels and active centers for recombination leading to different emissions. Further, the emission depends on the dopant concentration as well. The praseodymium-doped fluorapatite illustrated green emission at 545 nm and orange emission at 600 nm [52]. Europium/barium co-doped and F-substituted nHAp (HA@nFAp:Eu/Ba) showed high sensitivity in both computed tomography and fluorescence imaging [53]. Carbon dots/HAp/PVA (CDs/HA/PVA) dual-network (DN) hydrogel scaffold showed an excellent fluorescence in non-invasive monitoring field for the in vivo evaluation [54]. In vivo investigation is a challenging task; these advanced materials help in monitoring the cell viability and cell proliferation on implants without following supplementary way to understand cell interaction. Xing et al. developed heparin-coated Eu^{3+}-doped HAp nanoparticles (SH-Eu:nHAP) for bioimaging [55]. HAp nanorods tune color from blue to red and also emit white colors depending on the temperature, excitation wavelengths, etc. [56]. Optical responses, band gap, and emission behavior of materials vary on thermal treatments; further, thermal defects and production of active centers were responsible for the rapid/slow recombination of the electron and hole pairs. Hence, thermal-based luminescence is a fascinating process of emission with respect to various temperatures. However, thermally induced defects are not stable and returned to the ground state by emitting photons. Further, doping modifies the interatomic and intra-atomic transition states of basis during thermoluminescence. For instance, thermoluminescence of HAp doped with different percentages of lanthanum (La), Eu, gadolinium (Gd), and dysprosium (Dy) has been examined under the gamma radiation and (1 m%) Dy-doped samples demonstrated its capability to be used for gamma radiation dosimetry [57]. Cathodoluminescence and thermoluminescence nature of calcium phosphates were also investigated in the UV-IR range with the wavebands due to hydroxyl groups, nonbridging oxygen, etc. [58]. HAp and YAG:Ce ceramics were synthesized by Huang et al. at 850°C to fabricate white light-emitting diodes with phosphor in ceramics (PiCs) color converters in transmission mode [59]. So, these green diodes are useful in reducing the consumption of toxic materials (europium, cadmium etc.) and will guide researchers to develop various green-based diodes. Gd-dependent blue emission was observed on selenium (Se) and gadolinium (Gd) dual ions doped HAp nanoparticles under ultraviolet (UV) irradiation [60]. Copper-doped Sr-HAp was prepared by solid-state reaction $Sr_{10}(VO_4)_{6-x}(PO_4)_xO_2Cu_yH_{2-y-\delta}$ (x = 0–6; y = 0–0.24) as the x value decreases; copper-doped samples show intense blue emission [61]. In most of the cases, the PL emission was reduced due to the concentration quenching and non-radiative recombination of electron and hole pairs which evidently showed the variation of active centers in the matrix.

Europium-doped calcium phosphate apatite-based colloids possess narrow emission with long luminescence lifetimes suitable for nanoprobe as reported by Kattan et al. [62]. These colloids were stable over time and excite near visible or visible light domains. The excited states in the colloids were highly stable and electron decay time was slow. Further, non-radiative recombination centers might be far away from each other to reduce the bleaching effect. Mesoporous strontium ions doped HAp samples exhibited blue emission and sustained drug release [63]. The PL intensity of doped HAp was correlated to the amount of ibuprofen released [63]. Similarly, Yang et al. reported the red emission of europium-doped HAp and its PL intensity altered with the release of drug molecules [64]. This idea has many practical difficulties at *in vivo* level and could be addressed by developing advanced analysis. Thus, doped HAp nanostructures can be an ideal candidate for both bio-imaging and drug delivery. Still, there is a lack of fundamental and basic understanding of electrical and optical nature of doped HAp. The main focus of this chapter is to discuss few instances of metal ions doped HAp and its electrical and optical behavior. Further, the path that lead to the development of next generation advanced biomedical materials will also be examined.

2. Types of calcium phosphates

Calcium phosphates are found in the bone and teeth as the major inorganic constituent. Depending on the Ca/P ratio and structure, the phases of calcium phosphate are classified as tabulated in **Table 1**. Although these phases of calcium phosphate are different from each other by their chemical composition, but they are biocompatible, non-toxic, and osteoconductive in nature which have ability to stimulate tissue regeneration. The HAp and tricalcium phosphate (TCP) are the mostly used ceramics in biomedical applications among the phases of calcium phosphate. The combination of these two phases result in a new phase formation which was recognized as a biphasic calcium phosphate used in bone repair and replacement applications. The phases of calcium phosphate have their individual adsorption and resorption capacities.

S. No.	Phase	Abbreviation	Empirical formula	Ca/P ratio
1.	Calcium phosphate monohydrate	MCPM	$Ca(H_2PO_4)_2.H_2O$	0.5
2.	Monocalcium phosphate	MCP	$Ca(H_2PO_4)_2$	0.5
3.	Dicalcium phosphate	DCP	$CaHPO_4$	1.0
4.	Dicalcium phosphate dihydrate	DCPD	$CaHPO_4.2H_2O$	1.0
5.	Octacalcium phosphate	OCP	$Ca_8H_2(PO_4)_6.5H_2O$	1.33
6.	Tricalcium phosphate	TCP	$Ca_3(PO_4)_2$	1.5
7.	Amorphous calcium phosphate	ACP	$Ca_{10-x}H_{2x}(PO_4)_6(OH)_2$	1.2–2.2
8.	Calcium-deficient hydroxyapatite	CDHA	$Ca_9(HPO_4)(PO_4)_5(OH)$	1.5–1.67
9.	Hydroxyapatite	HAp	$Ca_{10}(PO_4)_6(OH)_2$	1.67
10.	Oxyapatite	OXA	$Ca_{10}(PO_4)_6O$	1.67
11.	Tetracalcium phosphate	TTCP	$Ca_4O(PO_4)_2$	2.0

Table 1.
Phases of calcium phosphate [65].

The solubility of calcium phosphate (CaPs) varies from each other and the *in vivo* degradation was foreseen in the order MCPM>TTCP>α-TCP > DCPD>DCP > OCP > β-TCP > CDHA>HAp [29]. Monocalcium phosphate monohydrate (MCPM) is soluble in water and is acidic in nature. Therefore, it cannot be used in the bone repair applications. The MCPM combined with α-TCP or β-TCP, makes it less soluble [65, 66]. Usually the MCPM has been used as fertilizer and commonly known as superphosphate fertilizer. The Monocalcium phosphate (MCP) was prepared by heating the MCPM at 100–110°C and is similar to the MCPM. The MCP has been rarely used due to its highly hygroscopic nature [67].

Dicalcium phosphate (DCP) is biocompatible and bioresorbable and has been used as bone cement [68, 69]. Dicalcium phosphate dihydrate (DCPD) also known as brushite can be easily synthesized and has osteoconductive property. It is a metastable material and can be converted to other phases DCP, OCP, CDHA, and TCP by varying the pH of the reactant solutions. The octacalcium phosphate (OCP) is responsible for the formation of teeth and bone. It crystallizes very slowly and is not suitable for bone cement application. The α-TCP and β-TCP are polymorphs having same chemical composition with different structures [70, 71]. The α-TCP's solubility is better than that of β-TCP but both are biocompatible, resorbable, and have been used as bone cement. Among the phases of CaPs, the HAp is more stable and highly crystalline in nature. When the HAp is heated above 900°C, it is converted to oxyapatite (OXA) in an inert atmosphere. The tetracalcium phosphate (TTCP) was prepared by heating the DCP and calcium carbonate at 1400°C with rapid cooling [72].

3. Electrical properties

HAp is a bioceramic having a high dielectric constant. Researchers have studied the impact of electric field on the HAp to understand the real part and imaginary part of the permittivity [37, 38]. These properties provide us an insight into the dielectric polarization of electric dipoles with respect to electric field. Further, the dielectric studies aid to understand *in vitro* electrical polarization. The respective real and imaginary part of permittivity grants dispersion of dipoles and energy dissipation. Some other parameters say temperature, experimental condition and dopants can influence and alter the dielectric properties. Doping sites and dopant's radius alter the electronic and orientation polarization, whereas co or tri-doping significantly affects the structure and phase, further, the dielectric properties of these materials might vary due to the rate of dipole relaxation. Generally, at low frequency alternating field, the dielectric constant is high and varies with increase in frequency. Nakamura et al. studied the polarization of HAp using direct current and showed that proton migrates along the columnar OH channel [38]. The polarized charge was high enough to improve biological activity. Usage of the electrical fields enabled the accelerated fracture healing in bones; however, it was slow in the case of long bone [72–74]. There are some reports on electrical stimulation which has been used to enhance the bone growth in spinal fusion [75, 76]. Further, it has been employed to treat osteonecrosis as well as osteoarthritis [77]. The dielectric constant of fluids and tissues in the bone and HAp is crucial for healing. The porosity of HAp plays a vital role for the local electrical field strength [78, 79]. Human bones also contain many elements such as magnesium, zinc, and strontium etc., so, the impact of the elements in the bone also play a vital role in the dielectric constant of bone. Further, it as well depends on the elemental size, concentration, and interrelated porosity.

For instance, doping of magnesium ions on HAp enhances the dielectric constant (**Figure 1A**) [30]. At low frequency, the dielectric constant was high due to ionic polarization; however, it was reduced by lagging of dipoles with respect to electric field. At low magnesium ions doping, the dielectric constant was low and almost equal to the dielectric constant of HAp. So, the low level doping did not highly polarize the ions in the direction of electric field and difficult to locate the dopant site position either at calcium site 1 or calcium site 2. As the Mg concentration increases, both the sites might be occupied and at low frequency the dipoles were strongly oriented, whereas it was disturbed at high frequency. Similarly, the cadmium-doped HAp revealed a higher dielectric constant in comparison with pure HAp. However, 40% of cadmium-doped HAp shows a decrease in the dielectric property. At 1 kHz frequency, the dielectric constant of HAp, doped samples 10 at.% Cd, 20 at.% Cd, 25 at.% Cd, 30 at.% Cd, and 40 at.% Cd were 6.75, 7.12, 8.16, 7.13, 7.26, and 6.24 respectively. At 40 at.% Cd, the structural change from hexagonal to monoclinic with varying crystallinity was responsible for the reduction in the dielectric constant [80]. In the case of silver-doped HAp, the dielectric constant was enhanced due to a high dipole polarization [81]. The dopant size varies the phase of HAp leading to amorphous or partial amorphization which completely modifies the local coordination and chemical potential. Horiuchi et al. revealed the two step relaxations of fluorine substituted HAp (F-HAp) [82]. They depicted that one step from 600 to 60 Hz and other 60 to 20 Hz in HAp which were analogous to the F-HAp. At low frequency, the electric dipoles are largely (L) relaxed, whereas at high frequency, the relaxation was small (S). Further, they calculated the activation energy of HAp and F-HAp as 0.63 and 0.62 eV, respectively, for one type of relaxation and it was independent of fluorine substitution. In case of other relaxation, the activation energy was significantly influenced by fluorine substitution due to the change in orientation of hydroxyl groups [82].

In the case of tungsten (W)-doped HAp, the relative permittivity was reduced up to 1 MHz and from 1 to 5 MHz the permittivity was constant [83]. The dielectric constant of W-doped HAp was high at low frequency due to the polarization of electronic, ionic, dipolar, and space charge. As the doping concentration increases, the dielectric constant was enhanced [83]. Thus, the dopants enhance spreading of the electromagnetic fields in the damaged bone sites or fractured area for rapid healing. Similarly, the other metal ions strontium [21], iron [26] etc., have been used as dopants in HAp to enhance dielectric property. A crucial and impressive part is how dielectric constant varies with concentration and with various dopants and the mechanism involved. The co-doping in HAp leads to the creation of many defects and alters the ionic polarization with respect to electric field. For instance, iron and zinc ions were co-doped in HAp at various concentrations (0.01, 0.05,

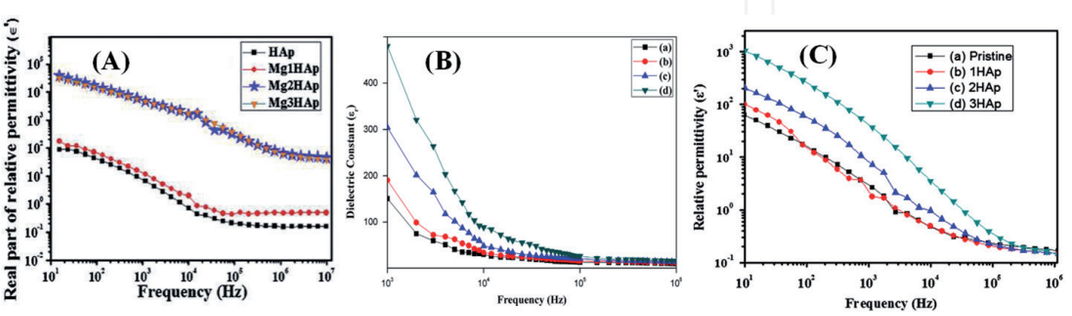

Figure 1.
(A) Real part of relative permittivity of HAp and Mg-doped HAp (reproduced from Ref. [30] with permission from Elsevier). (B) Dielectric constant of (a) FZH0, (b) FZH1 (0.01 M), (c) FZH2 (0.05 M) and (d) FZH3 (0.1 M) (reproduced from [35] with permission from Elsevier) and (C) The real part of relative permittivity as a function of frequency for (a) Pristine, (b) 1HAp (1×10^{15} ions/cm^2), (c) 2HAp (1×10^{16} ions/cm^2) and (d) 3HAp (1×10^{17} ions/cm^2) (reproduced from [84] with permission from Elsevier).

and 0.1 M) by ultrasonication. At higher concentration (FZH3) (0.1M), dielectric constant was greater (**Figure 1B**) compared to the other samples owing to the enhanced ionic polarization and strong orientation of dipoles at low frequency. As the frequency increases, the dielectric constant was reduced in all the samples due to lagging of the dipoles [35]. Generally, at low frequency, the value of dielectric is high due to slow relaxation of dipoles with high orientation. At high frequency, the dielectric constant was reduced due to strong re-alignment of dipoles with field [30, 83]. Further, it depends on the size of dopants, crystal structure, and concentration providing atomic site variations which enable the variations in the unit cell and crystal structure. Moreover, the dopants provide vacancies which affect space charge localization/delocalization. This facilitates the alterations in the dielectric constant. In case of the HAp structure, the hydroxyl ions aligned along c-axis parallel to calcium and phosphate $(PO_4)^{3-}$ ions favor high polarization of electric dipoles thereby increasing the ionic conduction [38]. Surface charge of HAp is another important parameter which assists the bone cell growth. The polarized surface of HAp had improved the osteobonding in canine bone tissues [39]. So, the electric properties have been employed to understand the cellular behavior on bone and to develop bone prostheses [38]. The surface charge of HAp depends on the porosity and dielectric strength. It can vary on low energy ion implantation which are capable of altering the surface properties without affecting the bulk properties of the materials. Nitrogen ions (N^{+1}) were implanted in HAp matrix with varying ion fluences 1×10^{15} (1HAp), 1×10^{16} (2HAp), and 1×10^{17} (3HAp) ions/cm^2 [84]. At higher ion fluence (3HAp), relative permittivity was significantly enhanced (**Figure 1C**) in comparison with other samples because of the higher ionic and space charge polarizations. The surface and subsurface of HAp were modulated on ion implantation altering the dipole polarization thereby leading to the variation in the surface charge of the samples. The polarization varies locally leading to dielectric strength modification at the surface, subsurface and at macro level. Hence, the surface charge can be tuned by different dopants, temperature, and frequency.

The variation of dielectric constant with frequency of pure and Fe-doped HAp, Mn-doped HAp, and Co-doped HAP sample at room temperature was examined by Panneerselvam et.al. [7]. The dielectric constant of the doped samples decreased sharply up to 10 kHz, and then reduced gradually with further increase in frequency. This difference in dielectric constant is due to the four types of polarization such as electronic polarization (frequencies up to 10^{16} Hz), ionic polarization (10^{13} Hz), orientation polarization (up to 10^{10} Hz), and space charge polarization or interfacial (up to 10^3 Hz) [7]. In all the samples, as the doping concentration increases, the dielectric constant was enhanced due to ionic polarization. The highest dielectric constant was exhibited by 5% MnHAp and the lowest by 5% CoHAp [7]. The dopants such as Fe, Mn, and Co possess different ionic radii and electronic cloud density. The variation of dielectric constant of the different metal ions doped HAp is due to the change in dipole strength, rate of dipole relaxation, and space charge polarization apart from ionic polarization. Tavangar et al. fabricated HAp-barium titanate (BT) scaffolds by cold isostatic pressing and sintering. As the BT concentration increases, the dielectric loss (D) of the composite was reduced due to the low porosities and higher densities of composite when compared with pure HAp. The 60 wt% BT had the lowest dielectric loss at 1 kHz. The dielectric constant of the 60 wt% BT–40 wt% HA composite was 46.50 which was the highest compared to the other composites due to the coupling of low-dielectric constant of HA with BT leading to a parallel polarization in the presence of phases with different weight percentages and electrical conductivity [11]. The ac frequency facilitated the coupling of the phases of materials leading to a synergic effect on the dipole polarization and orientation. Verma et al. studied the effect of concentration of

piezoelectric $Na_{0.5}K_{0.5}NbO_3$ (NKN) on dielectric and electrical properties of HAp in the range of temperature (30–500°C) at frequency 1 Hz to 1 MHz. The composite was prepared by solid state ceramic method and sintered at 1075°C for 2 h [13]. The experimental values of the dielectric constant are lower than those of calculated using theoretical models [13] due to the connectivity between HAp and NKN phases at the lower concentration of NKN in HAp matrix. The connectivity of matrix and secondary phase affects the electrical as well as mechanical properties of the composites. At low content of NKN, the HAp phases were connected in three-dimension whereas, no connectivity between NKN phases and 0–3 connectivity between NKN and HAp phases were observed. With enhancing content of NKN in the HAp matrix, the interaction between piezoelectric phases was increased. The calculated dielectric values of HAp-10 NKN, HAp-20 NKN, and HAp-30 NKN were 30.54, 38.71 and 50.29 respectively. The effective dielectric constant of HAp-10 NKN, HAp-20 NKN and HAp-30 NKN at 10 kHz (room temperature) were calculated to be 29.81, 35.32 and 42.046 respectively. The calculated and experimental values were significantly varied at high concentrations due to the combined involvement of complex parameters such as orientation and electronic The microstructure, densification, undetectable phases etc. play a vital role in determining the efficient dielectric constant of the composite system [13].

The ac conductivity measurements are used to study the mechanism of hopping and it is a complex phenomenon. Further, it depends on frequency and temperature [30]. The ac conductivity of Mg-doped HAp was enhanced compared to HAp (**Figure 2A**). There was low ac conductivity at low frequency due to the weak turnaround of ions with the electric field. However, it was increased at higher frequency on Mg-doped samples due to the complex array of ions and proton segregation along c-axis [30, 85]. Similar trend also noticed in W-doped HAp samples which linearly depend on the frequency range. Further, it obeyed the universal frequency power law. Towards understanding the mechanism of ac conductivity of the samples, the proverbial Jonscher equation ($\sigma_{ac} = \sigma_{dc} + B\omega^s$) was used [86], where B-constant, ω-angular frequency and s-frequency exponent. Using the slope of $\ln\sigma$ vs. $\ln\omega_{ac}$ and the s values were calculated as 1.0622, 1.0600, 1.0623, 1.0501, 1.0518, 1.0629, and 1.0534 for pure and 1, 5, 10, 20, 30, and 40% of W in HAp, respectively. Here, s is almost ≤1, revealing no measureable direct current conductivity and displays prompt hopping with a translational motion [83]. In the case of the Cd-doped HAp samples, the alternating current conductivity was enhanced from 10^{-10} to 10^{-5} s cm^{-1} with an increase in frequency. The frequency exponent(s) was

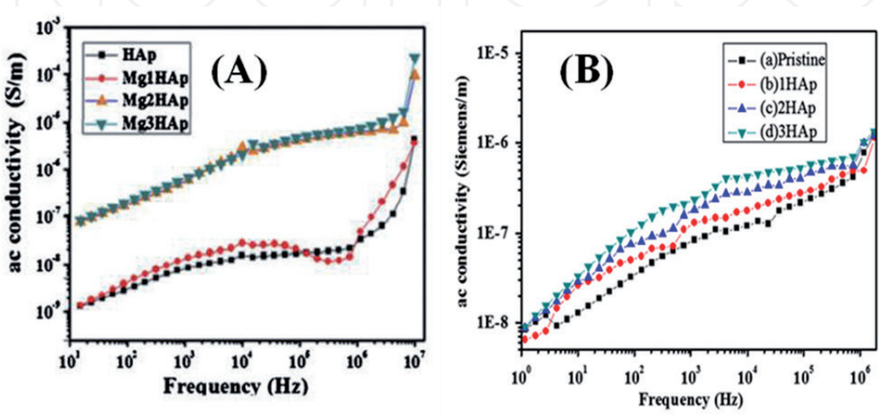

Figure 2.
(A) Ac conductivity as a function of frequency of HAp and Mg-doped HAp (reproduced from Ref. [30] with permission from Elsevier); and (B) The ac conductivity as a function of frequency for (a) Pristine, (b) 1HAp, (c) 2HAp and (d) 3HAp (reproduced from [84] with permission from Elsevier).

determined from the slope of logσ vs. logω and its value equal to 1 for the samples [80]. Eventually, it displays a lack of direct current conductivity [87]. Similar, s value was realized for the Te-doped HAp samples however, their ac conductivity enhanced at low concentration due to $s \geq 1$ leading to localized hopping. At higher concentration, it was reduced due to $s \leq 1$ leading to translation motion with a rapid hopping motion [88]. Ion implantation could also be employed to alter the ac conductivity, without using expensive and toxic chemicals. It can precisely modulate the ac conductivity up to a particular depth. Nitrogen ions implanted samples demonstrated higher ac conductivity at higher frequency owing to the strong arrangement of complex ions compared to pristine (**Figure 2B**). However, it was less at low frequency due to the weak turnover of ions [84].

4. Optical properties

The interaction of light on materials leads to transmission, absorptions and reflection. These parameters depend on refractive index, wavelength, dielectric constant, and dopants. Dopants play a vital role in creating the abundant defects/vacancies in the lattice of materials. When light interacts on the bound charges of the materials, they either transmit or reflect back. The structure and phase of HAp varied depending on the type of dopant [80] which also alters the optical properties of HAp. The optical properties of HAp were enhanced by developing smaller grains and low porosity in the HAp matrix. It is an optically anisotropic material and possesses a refractive index in the range 1.644 and 1.651 depending on light polarization and direction of propagation [89]. A highly transparent HAp nanosized grains were used to observe *in vivo* interactions with proteins/cells [90, 91]. For a proper insight of the optical properties, intrinsic correlated parameters/quantities say crystalline structure, dispersion of phonon, band structure, dielectric response, band gap, etc. are required. Density functional theory displays a local or semi local exchange-correlation interaction of HAp providing a band gap between 4.5 and 5.4 eV depending on the type of valence states [92, 93]. However, the (semi) local exchange-correlation underestimates the band gap of HAp, and thus its value is above 5.5 eV [94]. So, the defect free HAp is transparent to visible light under middle or far ultraviolet illumination having a band gap >6 eV. Interesting point to note is that the dopants produce defects level in between conduction band and valence band.

For instance, the thenoyltrifluoroacetonate (TTA)- and europium (Eu)-doped HAp were used to enhance transmission spectra by 20% compared to PMMA. The TTA shows a red shift and the transmission edge from 275 to 375 nm. Both the TTA and HAp mixture restrict the formation of PMMA clusters improving the transparency. In this case, the absorption and scattering losses were introduced by the TTA and the HAp nanoparticles [95]. The other example, Cd-doped HAp showed enhanced reflectivity at the Cd (40 at.%) due to the structural transformation to the monoclinic phase. Further, it alters the refractive index of the samples as well [80]. At a particular atomic percentage, the structural transformation occurred affecting the electronic polarization thereby, altering the reflectivity. In the case of erbium doping in HAp, seven absorption bands were noticed [43]. The bands observed at 1520, 980, 803, 657, 524, 490, and 448 nm corresponding to the electronic transitions from ground state $^4I_{15/2} \rightarrow {}^4I_{13/2}$, $^4I_{15/2} \rightarrow {}^4I_{11/2}$, $^4I_{15/2} \rightarrow {}^4I_{9/2}$, $^4I_{15/2} \rightarrow {}^4F_{9/2}$, $^4I_{15/2} \rightarrow {}^2H_{11/2}$, $^4I_{15/2} \rightarrow {}^4F_{7/2}$, and $^4I_{15/2} \rightarrow {}^4F_{3/2}$, respectively [92]. Among all the transitions, the $^4I_{15/2} \rightarrow {}^2H_{11/2}$ transition had the highest intensity due to the hypersensitive transition [92]. Further, the peaks were broadened inhomogeneously due to the f-f

interactions of Er^{3+} ions [96]. As the erbium doping concentration increases, the intensity of the peaks increased due to the replacement of Ca^{2+} by Er^{3+} ions. Further, there was a blue shift observed on the doped HAp due to the reduced particle size [97]. The Er-HAp samples possess direct band gap (n = 1/2) so band to band transitions was allowed. As the erbium doping concentration increased, the band gap was enhanced to 4.46 eV from 4.02 eV. Hence the structure, phase, defects and particle size of HAp are the key parameters to alter either the absorption or reflection. Further, the symmetry of the HAp also plays a predominant role in modifying the electronic polarization and dielectric constant.

Apurba et al. studied the optical response of HAp films of various thicknesses on amorphous SiO_2 substrates [98]. All the films showed 75–96% transparency in the visible region. There are two regions noticed, one is absorption and other a transparent oscillating region. Below 300 nm, the transmittance of the HAp films displayed robust absorption. When the film thickness enhances, the absorption edge was shifted to higher wavelength in turn altering electronic polarization Thus, these films revealed a strong absorption in UV region and transparency in the visible regions as well. The band gap of the varying thickness of HAp thin films was in the range 5.25–4.67 eV due to an increase in crystallinity and grain size. The band gap of thin films is similar to the band gap of bulk HAp (in the range of 5.4 to 4.51) [99]. For annealed films, the refractive indices were augmented with an increase in the film thickness [98]. Flores et al. reported that using the Kubelka-Munk function through the maximum of the first derivative, the absorption edge values were 5.62, 4.74 and 4.6 eV which correspond respectively to TbW0 [calcium-deficient (CD) HAp], TbW10 (terbium 10%-doped CDHA), and TbW12 (terbium 20%-doped CDHA) [100]. The optical band gap values of the TbW0, TbW10 and TbW12 samples were 5.41, 4.49 and 4.38 eV respectively. This demonstrates that as the Tb increases, the band gap was reduced. Here the host matrix having calcium vacancies was considered as n-type, whereas the Tb acts as a p-type dopant. When the Tb ions substitute at that calcium site then the electrons were delocalized to conduction band. Further, in the case of the TbW10 and TbW12 samples, the band gap was reduced. From the UV photoelectron spectra, the valence band energies of Ev0 (TbW0), Ev1 (TbW10) and Ev2 (TbW12) were 3.33, 2.55 and 2.40 eV, respectively [100]. It exhibits a decrease in the valence band at the higher concentration of Tb and varies Fermi level of the samples.

Feng et al. studied the drug adsorption capacity of HAp using absorption spectra [44, 101]. The respective drug adsorption capacity of the undoped HAp nanorod and the Eu^{3+}/Gd^{3+} HAp was 653.5 and 841.4 mg/g. The interaction of the dopants with drug molecules might be strong due to the presence of oxygen vacancies and atomic defects which pave a path for sustained or rapid release of drug molecules. This revealed that the doped nanorods displayed a high drug adsorption compared to undoped sample with a reduced absorbance. The size of the dopant and its doping concentration play a predominant role in modifying the crystal structure thereby the Fermi level position gets altered leading to the enhancement or decrease of the band gap. When photon interacts with the material, either high absorbance or transmission of photons occurs due to the variation in energy levels of defects or vacancies. The optical response of the doped HAp is not only dependent on material property and type of dopant (drug or organic molecules) but also on the type of wavelength used. Moreover, different wavelengths have distinct capability of light reflection, absorbance, and transmission as well.

The carbon-based HAp showed enhanced optical absorption. N-doped carbon dots (N-CDs) revealed absorption at about 240 and 340 nm, due to the $\prod$–$\prod^*$ transition of C = C and $\prod$–$\prod^*$ transition of C = O and C–N/C = N, respectively [56].

In the case of HAp:Eu,Gd, the absorption at 200–280 nm due to the wide band gap of HAp with a peak (395 nm), was assigned to the intrinsic 4f-4f transition absorption of Eu [56] confirming the incorporation of Eu into HAp. The absorption of N-CDs/HAp:Eu,Gd was superior than single N-CDs and HAp:Eu,Gd and its band edge shifted to 550 nm due to the porous structure and multiple reflection [47]. The CDs based system could be used as a stable bioimaging candidate. Ni^{2+}-doped calcium-lithium hydroxyapatite (CLHA) nanopowders were synthesized by mechanochemical synthesis by Reddy et al. [50]. The spectra of these powder possess four absorption band at 420, 718, 794, and 1189 nm attributed to the transitions of $^3A_{2g}(F) \rightarrow {}^3T_{1g}(P)$, $^3T_{1g}(F)$, $^1E_{1g}(D)$ (spin-forbidden transition), and $^3T_{2g}(F)$, respectively [50]. The chemical potential of the CLHA is drastically affected leading to the modification of conductivity and dielectric properties. Iron, manganese, and cobalt ions doped HAp possess direct band gap (index number n = 1/2). The band gap of 5% Co-doped HAp was higher than Fe, Mn ions doped samples [7]. The band gaps were modified due to the presence of defect energy levels which shift Fermi level toward the valence or conduction band.

5. Photoluminescence

The PL of HAp depends on the defect energy level formation, structure, and size of the nanoparticle. Moreover, its band gap is above 5.5 eV, when dopants added to HAp matrix, the band gap perhaps vary due to the formation of many defects energy levels in between valence and conduction band. When the HAp nanostructure was excited by different wavelengths, electrons were accordingly excited to the higher states sometimes, these electrons recombine with holes promptly to produce radiative emission. However, in some cases, the emission might be non-radiative. Proper understanding of the effect of dopant is required to create either light active or inactive centers which enable emission at different wavelengths. However, it also depends on the excitation wavelength as well. The defects energy level formation is a complex phenomenon containing the associated band position and the band bending process. It as well depends on the size, phase and atomic arrangements. In order to reduce non-radiative emission, the doping concentration must be properly tuned to avoid the occurrence of concentration quenching; otherwise, abundant non-radiative centers are facilitated [34].

Addition of sodium hydroxide (NaOH) varies PL of Sr-HAp samples [102]. By varying NaOH content, the shape of the spectra did not change drastically; however, the intensities vary significantly. The Sr-HAp sample (0.15 g NaOH) displays the strongest emission and the weakest intensity was at 0.40 g NaOH due to the variation in luminescent centers. Here, neither Sr^{2+} nor PO_4^{3-} is responsible for the luminescence but it was due to the carbon and oxygen related active electronic defect centers on the host matrix [102]. Some reports are available for the self-activated luminescence due to the addition of trisodium citrate which enables the creation of carbon monoxide impurities [103]. In the case of the Tb-doped samples, the excitation peaks of TbW10 (terbium 10% CDHA) and TbW12 (terbium 20% CDHA) were matched with that of CDHA. Further, the vacancies and carbonate radicals act as acceptor chromophores and terbium ions as donor chromophores. The interaction of chromophores leads to a non-radiative relaxation through defects and impurities in each sample [100]. Two different wavelengths (255 and 264 nm) were used for excitation of the samples. The emission peaks were associated with $^5D_4 \rightarrow {}^7F_6$ (489 nm), $^5D_4 \rightarrow {}^7F_6$ (544 nm), $^5D_4 \rightarrow {}^7F_4$ (585 nm), and $^5D_4 \rightarrow {}^7F_3$ (622 nm) due to intraconfigurational 4f-5d transitions of the Tb^{3+} ion. At the 544 nm, a high intense green light emission was noticed in the doped samples

(TbW10) [104, 105]. There was a weak contribution of the PL emission from the host matrix of both samples and displayed a deformation of the peak shape with a small shift in the peaks $^5D_4 \rightarrow {}^7F_6$ and $^5D_4 \rightarrow {}^7F_4$ transitions. The emission from TbW10 was high due to chemical composition, self-activated CDHA, whereas at higher Tb doping (TbW12), the intensity was reduced due to concentration quenching leading to non-radiative relaxation [100].

Yang et al. reported the broad excitation spectrum at 250 nm due to the charge transfer between europium and oxygen ions and further, small peaks were noticed at longer wavelength due to f-f transitions of Eu^{3+} [28]. It was monitored by $^5D_0 \rightarrow {}^7F_2$ transition at 612 nm. The two peaks were prominently noticed at $^5D_0 \rightarrow {}^7F_1$ (590 nm) and $^5D_0 \rightarrow {}^7F_2$ (612 nm). Even the IBU-loaded europium-doped HAp samples display a clear PL spectrum and it can be tracked by the luminescence intensity. The fascinating part is how the PL intensity varies with release rate of drug molecules. As the cumulative release rate increases, the PL intensity enhances and reached maximum when all drug molecules were released completely. The organic groups of the IBU highly quenched the emission due to europium in the IBU-Eu:HAp. The IBU creates high non-radiative centers in the matrix. However, the release of IBU augments with a weakening of quenching effect which was confirmed by enhanced PL intensity. Thus, it was used as a potential probe for monitoring the drug release [28].

In the case of dual ions doped samples, the europium/gadolinium dual-doped HAp nanorods showed a maximum excitation peak at 394 nm [44]. There was no significant emission on the co-doping of europium (Eu^{3+})/gadolinium (Gd^{3+}) compared to the lone europium doping. However, the PL intensity was altered and four emission peaks were noticed at 590, 615, 650, and 699 nm [44]. The prominent peak was identified at 615 nm due to $^5D_0 \rightarrow {}^7F_2$ transition within Eu^{3+} ions. The other PL peaks were observed at 590, 650, and 699 nm owing to their respective $^5D_0 \rightarrow {}^7F_1$, $^5D_0 \rightarrow {}^7F_3$, and $^5D_0 \rightarrow {}^7F_4$ transitions. As the doping concentration of europium increases, the PL emission intensity was enhanced. The highest PL intensity occurred in 5 mol% Eu^{3+} but with an enhanced intensity compared to the dual doped samples. The PL intensity was higher at the doping ratio of Eu^{3+} to Gd^{3+} (1:2) than the ratio 1:1. On UV irradiation, the dual doped samples displayed a robust red emission from powder as well as from powder dispersed solution [44]. So, the PL intensity depends on the phase, particle size and defect based active centers which absolutely alter either the inter- or intra band transition and emission.

In the case of Mg ions doping on HAp, the PL intensity was enhanced accompanied by a modification of the spectra. At higher Mg concentration, the peak was reduced due to weak radiative recombination [30]. Further, the defects create many active centers for non-radiative recombination and the centers might be very close to each other for a rapid decrease in the PL intensity. As the Mg and Ag ions in HAp augments, the PL intensity was enhanced, however, as the concentration raises, the intensity was reduced (**Figure 3A**) [34]. With further increase in co-doping, the PL intensity was enhanced but lesser than the lowest concentration of co-doping [34]. A similar emission was also seen in the iron and zinc co-incorporated HAp samples, but as the co-doping increases, the PL intensity was reduced (**Figure 3B**) [35]. So, the PL intensities were tuned by varying co-doping concentration which might alter the radiative recombination active center in the HAp matrix. Ion implantation is one of the effective routes to dope a particular element at the desired depth and varying defects energy level to tune the PL intensity. Nitrogen ion implantation enhanced the PL emission of HAp [84]. As the ion fluence increases, the PL intensity was enhanced due to the radiative recombination of electron-hole pair without the influence of concentration quenching effect (**Figure 3C**) [84]. There are reports on different synthesis routes for doping of various elements on HAp viz., microwave-assisted

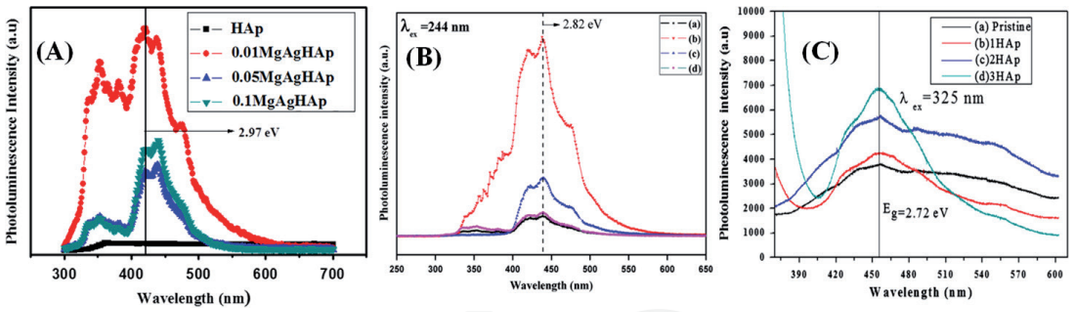

Figure 3.
(A) Photoluminescence spectra of HAp and magnesium and silver ions co-incorporated HAp samples (reproduced from [34] with permission from Elsevier), (B) Photoluminescence spectra of (a) FZH0, (b) FZH1, (c) FZH2 and (d) FZH3 (reproduced from [35] with permission from Elsevier) and (C) Photoluminescence of (a) pristine, (b) 1HAp, (c) 2HAp and (d) 3HAp (reproduced from [84] with permission from Elsevier).

route followed by ion implantation which is similar to dual ions doping [106]. However, the implantation was used to create/dope ions on the surface and subsurface with associated defects/vacancies without disturbing bulk properties of HAp. For instance, nitrogen ion implantation on magnesium ion incorporated HAp samples demonstrated that at low fluence of nitrogen, the PL intensity was enhanced [106]. However, at high fluence, the intensity was reduced due to concentration quenching and high non-radiative centers created on the surface. The PL intensity of unmodified Mg-doped HAp decreased drastically compared to the surface modified samples [106]. In the case of polymer (polyvinyl alcohol) doping in HAp, the PL intensity was raised [107] and the highest PL intensity was noticed at higher concentration due to the formation of abundant active sites created by the carbon and oxygen radicals in the polymer chains. So, the PL signal could be enhanced by optimizing the doping concentration, varying the band gap and creating active recombination defect sites and vacancies.

Machado et al. studied the photoluminescence of HAp nanorods at different excitation wavelengths (380 to 680 nm) [56]. They demonstrated a shift of emission from blue to red owing to the absence of the short wavelength emission with an increase in the excitation. Near-UV excitation, the intensity was higher with blue/green emissions. Eventually, the best emission intensity was in the range 330 to 430 nm [56]. Erbium-ytterbium (Yb)-molybdenum (Mo) tri-doped HA/β-TCP phosphor prepared by solid-state reaction was examined for intense green upconversion (UC) emission [51]. M5 ((0.5% mol) Er-(10% mol) Yb-(8% mol) Mo tri-doped HA/β-TCP) showed green emission intensity 650 times than that of the M1 (0.5% mol Er-doped HA/β-TCP), M2 ((0.5% mol) Er-(10% mol) Yb co-doped HA/β-TCP) due to energy transfer from $^{2}F_{7/2}$, $^{3}T_{2}$ > state of Yb^{3+} – MoO_4^{2-} dimer to the $^{4}F_{7/2}$ of Er^{3+} ions. Further, red emission was weak because of feeble absorption cross-section of $^{4}I_{13/2}$ and the green emission band can be controlled by the Mo^{6+} doping concentrations. It aids to use the material for bioimaging application [51]. N-doped carbon dots/HAp:Eu,Gd (N-CDs/HAp:Eu,Gd) composite were studied [47] and the PL spectra of N-CDs/HAp:Eu,Gd simultaneously revealed the emission from N-CDs and HAp:Eu,Gd on single wavelength excitation. The PL emission depicted no shift under different wavelengths revealing excitation independent emission. It clearly shows that the electronic structure of N-CDs and Eu ions were not affected during the synthesis. So, both the N-CDs and HAp:Eu,Gd were preserved. The PL lifetime of both N-CDs/HAp:Eu,Gd and N-CDs illustrated a single exponential decay but the lifetime decreased from 11.7 ns (N-CDs) to 5.6 ns (N-CDs/HAp:Eu,Gd) owing to the photogenerated charges [47]. Further, it could be used for bioimaging with distinct differentiation of colors due to different emission from carbon dots and doped HAp samples. Polymer/inorganic based structures can also affect the PL. Karthikeyan et al.

described the formation of core-shell structures on argon ion implanted polymer-based zinc ions incorporated HAp and reported that the zinc ions and the polymer lead to formation of many defects which in turn produces additional energy states. The PL intensity at the lower fluence samples (1×10^{14} ions/cm^2) showed enhancement in the PL intensity due to the presence of higher radiative active centers. On increasing the fluence viz., 1×10^{15} ions/cm^2 and 1×10^{16} ions/cm^2, the PL intensity was decreased owing to the formation of more non-radiative centers [108]. The incorporation of metal ions such as iron not only play a major role in tailoring the optical properties but also when exposed to magnetic field, they tend to change their morphologies depending on the magnetic field strength and have potential biological application such as protein absorption [109]. It could also lead to the development of magnetic based prolonged PL emission. Hence, the structure and morphology play a prominent role in altering the radiative/non-radiative recombination sites which can be correlated to the PL intensity decay.

6. Summary and future outlook

The effect of electric field, electromagnetic dispersion, dielectric relaxation and correlated structural variation of the doped HAp samples was discussed. The role of hydroxyl ions, frequency exponent and the mechanism of ac conductivity by translation and hopping motion in the doped HAp samples were elaborated. Further, the electrical studies showed that the polarized surface charge either positive or negative, could alter the growth of bone cells on HAp. The surface charge, microstructure, densification, porosity, phase, electrical dipole reversal and its strong orientation were responsible for the enhancement in the dielectric constant of the doped HAp samples. The optical response depends on the dopant size and its concentration and associated phase transformation. The formation of different energy levels and electronic level transitions on doping enabled the tuning of the PL intensity and multi-color emissions which are independent of the excitation wavelength. The drug-loaded doped HAp samples and their PL intensity were correlated to the rate of drug release. Thus, the europium ion-doped HAp behaves as a one-dimensional nanoprobe for tracking the drug release. Further, different synthesis routes, doping, and co-doping are capable of generating new energy levels between conduction and valence band. Moreover, it was understood that the respective radiative and non-radiative emission were due to the activated luminescent centers and the concentration quenching of the doped samples.

Electro-opto biomaterials could be developed for the rapid healing of bone defects and fracture owing to the enhanced bone cell proliferation and growth. Current, *in vitro* and *in vivo* analysis routes must be improved further to control infection and to enhance the cell growth after implantation. To have an exact biomimicking of the bone, multielemental incorporation of the HAp is essential. Still, there is a lack of advanced analysis technique to have an insight of the surface charge interaction with the bone cells and how these charges assist the precipitation, mineralization, and growth of bone tissues. Solar/photon and magneto/light-based advanced biomaterials need to be developed for rapid healing and recovery.

Acknowledgements

The authors thank AMSS, IGCAR, Kalpakkam, Tamil Nadu, for providing the lab facilities to carry out the characterization of the samples.

Author details

Kumaravelu Thanigai Arul[1*], Jayapalan Ramana Ramya[2] and Subbaraya Narayana Kalkura[3*]

1 Energy and Biophotonics Laboratory, Department of Physics, AMET (Deemed to be University), Chennai, Tamil Nadu, India

2 National Centre for Nanoscience and Nanotechnology, University of Madras, Guindy Campus, Chennai, Tamil Nadu, India

3 Crystal Growth Centre, Anna University, Chennai, Tamil Nadu, India

*Address all correspondence to: thanigaiarul.k@gmail.com and kalkura@yahoo.com

References

[1] Soballe K, Larsen ST, Gelineck J, Fruensgaard S, Hansen ES, Ryd L, et al. Migration of hydroxyapatite coated femoral prostheses. Journal of Bone and Joint Surgery. 1993;**75-B**:681-687

[2] Chang YL, Stanford CM, Wefel JS, Keller JC. Osteoblastic cell attachment to hydroxyapatite-coated implant surfaces in vitro. The International Journal of Oral & Maxillofacial Implants. 1999;**14**:239-247

[3] Schilephake H. Bone growth factors in maxillofacial skeletal reconstruction. International Journal of Oral and Maxillofacial Surgery. 2002;**31**:469-484

[4] Das A, Pamu D. A comprehensive review on electrical properties of hydroxyapatite based ceramic composites. Materials Science and Engineering: C. 2019;**101**:539-563

[5] Hendi AA, Yakuphanoglu F. Dielectric and ferroelectric properties of the graphene doped hydroxyapatite ceramics. Journal of Molecular Structure. 2020;**1207**:127734

[6] Baskar S, Elayaraja K, Nivethaa EAK, Ramya JR, Sankar VD, Catalani LH, et al. Thermally modified iron-inserted calcium phosphate for magnetic hyperthermia in an acceptable alternating magnetic field. Physical Chemistry B. 2019;**123**:5506-5513

[7] Panneerselvam R, Anandhan N, Gopu G, Roselin AA, Ganesan KP, Marimuthu T. Impact of different transition metal ions in the structural, mechanical, optical, chemico-physical and biological properties of nanohydroxyapatite. Applied Surface Science. 2020;**506**:144802

[8] Ibrahim M, Dawood A. Influence of doping chromium ions on the electrical properties of hydroxyapatite. Egyptian Journal of Basic and Applied Sciences (EJBAS). 2020;**7**:35-46

[9] Sundarabharathi L, Ponnamma D, Parangusan H, Chinnaswamy M, Maadeed MAAA. Effect of anions on the structural, morphological and dielectric properties of hydrothermally synthesized hydroxyapatite nanoparticles. SN Applied Sciences. 2020;**2**:94

[10] Nayak B, Misra PK. Recognition of the surface characteristics and electrical properties of a nanocrystalline hydroxyapatite synthesized from *Pila globosa* shells for versatile applications. Materials Chemistry and Physics. 2019;**230**:187-196

[11] Tavangar M, Heidari F, Hayati R, Tabatabaei F, Vashaee D, Tayebi L. Manufacturing and characterization of mechanical, biological and dielectric properties of hydroxyapatite-barium titanate nanocomposite scaffolds. Ceramics International. 2020;**46**:9086-9095

[12] Khouri AE, Zegzouti A, Elaatmani M, Capitelli F. Bismuth-substituted hydroxyapatite ceramics synthesis: Morphological, structural, vibrational and dielectric properties. Inorganic Chemistry Communications. 2019;**110**:107568

[13] Verma AS, Kumar D, Dubey AK. Dielectric and electrical response of hydroxyapatite – $Na_{0.5}K_{0.5}NbO_3$ bioceramic composite. Ceramics International. 2019;**45**:3297-3305

[14] Helen S, Kumar AR. Study of structural, mechanical and dielectrical properties of ions doped apatite for antibacterial activity. Materials Chemistry and Physics. 2019;**237**:121867

[15] Obaid A, Omer K, Mai HSA, Zahran HY, Kilany M, Yahia IS, et al. Antimicrobial activity of Ga-doped hydroxyapatite nanostructures: Synthesis, morphological,

spectroscopic, and dielectric properties. Journal of Biomaterials and Tissue Engineering. 2019;**9**:881-889

[16] Nihmath A, Ramesan MT. Preparation, characterization, thermal, and electrical properties of chlorinated ethylene propylene diene monomer/ hydroxyapatite nanocomposites. Polymer Composites. 2016;**39**:1-8

[17] Horiuchi N, Madokoro K, Nozaki K, Nakamura M, Katayama K, Nagai A, et al. Electrical conductivity of polycrystalline hydroxyapatite and its application to electret formation. Solid State Ionics. 2018;**315**:19-25

[18] Sanchez AG, Prokhorov E, Barcenas GL, García AGM, Y, Muñoz EMR, Raucci MG, Buonocore G. Chitosan-hydroxyapatite nanocomposites: Effect of interfacial layer on mechanical and dielectric properties. Materials Chemistry and Physics. 2018;**217**:151-159

[19] Rivas M, Valle LJD, Armelin E, Bertran O, Turon P, Puiggalí J, et al. Hydroxyapatite with permanent electrical polarization: Preparation, characterization, and response against inorganic adsorbates. ChemPhysChem. 2018;**19**:1746-1755

[20] Yun J, Qin W, Benthem KV, Thron AM, Kim S, Han YH. Nanovoids in dense hydroxyapatite ceramics after electric field assisted sintering. Advances in Applied Ceramics. 2018;**117**:376-382

[21] Lakshmanaperumal S, Mahendran C. Structural, dielectric, cytocompatibility, and in vitro bioactivity studies of yttrium and strontium co-substituted nano-hydroxyapatite by sol–gel method. Journal of Sol-Gel Science and Technology. 2018;**88**:296-308

[22] Maiti M, Sarkar D, Liu S, Xu S, Maiti B, Paul K, et al. Tungsten doped hydroxyapatite processed at different temperatures: Dielectric behaviour and anti-microbial properties. New Journal of Chemistry. 2018;**42**:16948-16959

[23] Yamashita K, Oikawa N, Kitagaki K, Umegaki T. Acceleration and deceleration of bone-like crystal growth on ceramic hydroxyapatite by electrical poling. Chemistry of Materials. 1996;**8**:12697-12700

[24] Ueshima M, Tanaka S, Nakamura S, Yamashita K. Manipulation of bacterial adhesion and proliferation by surface charges of electrically polarized hydroxyapatite. Journal of Biomedical Materials Research. 2002;**60**:578-584

[25] Ohgaki M, Kizuki T, Katsura M, Yamashita K. Manipulation of selective cell adhesion and growth by surface charges of electrically polarized hydroxyapatite. Journal of Biomedical Materials Research. 2001;**57**:366-373

[26] Mercado DF, Magnacca G, Malandrino M, Rubert A, Montoneri E, Celi L, et al. Paramagnetic iron-doped hydroxyapatite nanoparticles with improved metal sorption properties. A bioorganic substrates-mediated synthesis. ACS Applied Materials & Interfaces. 2014;**6**:3937-3946

[27] Silvia P, Monica M, Monica S, Michele I, Alessio A, Martina G, et al. Magnetic labelling of mesenchymal stem cells with iron-doped hydroxyapatite nanoparticles as tool for cell therapy. Journal of Biomedical Nanotechnology. 2016;**12**:909-921

[28] Stanica V, Janackovic D, Dimitrijević S, Tanasković SB, Mitrić M, Pavlović MS, et al. Synthesis of antimicrobial monophase silver-doped hydroxyapatite nanopowders for bone tissue engineering. Applied Surface Science. 2011;**257**:4510-4518

[29] Trujillo NA, Oldinski RA, Ma H, Bryers JD, Williams JD, Popat KC.

Antibacterial effects of silver-doped hydroxyapatite thin films sputter deposited on titanium. Materials Science and Engineering: C. 2012;**32**:2135-2144

[30] Arul KT, Elayaraja K, Manikandan E, Bhalerao GM, Chandra VS, Ramya JR, et al. Green synthesis of magnesium ion incorporated nanocrystalline hydroxyapatite and their mechanical, dielectric and photoluminescence properties. Materials Research Bulletin. 2015;**67**:55-62

[31] Ziani S, Meski S, Khireddine H. Characterization of magnesium-doped hydroxyapatite prepared by sol-gel process. International Journal of Applied Ceramic Technology. 2014;**11**:83-91

[32] Nan K, Wu T, Chen J, Jiang S, Huang Y, Pei G. Strontium doped hydroxyapatite film formed by micro-arc oxidation. Materials Science and Engineering: C. 2009;**29**:1554-1558

[33] Avci M, Yilmaz B, Tezcaner A, Evis Z. Strontium doped hydroxyapatite biomimetic coatings on Ti6Al4V plates. Ceramics International. 2017;**43**:9431-9436

[34] Arul KT, Ramya JR, Bhalerao GM, Kalkura SN. Physicochemical characterization of the superhydrophilic, magnesium and silver ions co-incorporated nanocrystalline hydroxyapatite, synthesized by microwave processing. Ceramics International. 2014;**40**:13771-13779

[35] Ramya JR, Arul KT, Elayaraja K, Kalkura SN. Physicochemical and biological properties of iron and zinc ions co-doped nanocrystalline hydroxyapatite, synthesized by ultrasonication. Ceramics International. 2014;**40**:16707-16717

[36] Hoepfner TP, Case ED. The porosity dependence of the dielectric constant for sintered hydroxyapatite. Journal of Biomedical Materials Research. 2002;**60**:643-650

[37] Bowen CR, Gittings J, Turner IG, Baxter F, Chaudhuri JB. Dielectric and piezoelectric properties of hydroxyapatite-$BaTiO_3$ composites. Applied Physics Letters. 2006;**89**:132906

[38] Nakamura S, Takeda H, Kimihiro U. Proton transport polarization and depolarization of hydroxyapatite ceramics. Journal of Applied Physics. 2001;**89**:5386

[39] Kobayashi T, Nakamura S, Yamashita K. Enhanced osteobonding by negative surface charges of electrically polarized hydroxyapatite. Journal of Biomedical Materials Research. 2001;**57**:477-484

[40] Feng JQ, Yuan HP, Zhang XD. Promotion of osteogenesis by a piezoelectric biological ceramic. Biomaterials. 1997;**18**:1531-1534

[41] Nakamura S, Kobayashi T, Yamashita K. Extended bioactivity in the proximity of hydroxyapatite ceramic surfaces induced by polarization charges. ournal of Biomedical Materials Research. 2002;**61**:593-599

[42] Popa CL, Ciobanu CS. Synthesis and characterization of fluorescent hydroxyapatite. Romanian Reports in Physics. 2016;**68**:1170-1177

[43] Ammar ZA, Muhammed A, Goh YF, Rafiq M, Kadir A, Abdolahi A, et al. Structural characterization, optical properties and in vitro bioactivity of mesoporous erbium-doped hydroxyapatite. Journal of Alloys and Compounds. 2015;**645**:478-486

[44] Feng C, Peng H, Zhu YJ, Wu J, Zhang CL, Cui DX. The photoluminescence, drug delivery and imaging properties of multifunctional Eu^{3+}/Gd^{3+} dual-doped

hydroxyapatite nanorods. Biomaterials. 2011;**32**:9031-9039

[45] Baldassarre F, Altomare A, Corriero N, Mesto E, Lacalamita M, Bruno G, et al. Crystal chemistry and luminescence properties of Eu-doped polycrystalline hydroxyapatite synthesized by chemical precipitation at room temperature. Crystals. 2020;**10**:250

[46] Li L, Li D, Zhao W, Cai Q, Li G, Yu Y, et al. Composite resin reinforced with fluorescent europium-doped hydroxyapatite nanowires for in-situ characterization. Dental Materials. 2020;**36**:e15-e26

[47] Chang Q, Xu W, Chen Q, Xue C, Li N, Yang J, et al. One step synthesis of N-doped carbon dots/hydroxyapatite:EuGd composite with dual-emissive and solid-state photoluminescence. Applied Surface Science. 2020;**508**:144862

[48] Kolesnikov IE, Nikolaev AM, Lähderanta E, Frank-Kamenetskaya OV, Kuz'mina MA. Structural and luminescence properties of Ce^{3+}-doped hydroxyapatite nanocrystalline powders. Optical Materials. 2020;**99**:109550

[49] Zhang X, Xing Q, Liao L, Han Y. Effect of the fluorine substitution for –OH group on the luminescence property of Eu^{3+} doped hydroxyapatite. Crystals. 2020;**10**:191

[50] Reddy CV, Ravindranadh K, Ravikumar RVSSN, Shim J. A novel green-emitting Ni^{2+}-doped Ca-Li hydroxyapatite nanopowders: Structural, optical, and photoluminescence properties. Journal of Materials Science: Materials in Electronics. 2020;**31**:5097-5106

[51] Van HN, Vu NH, Pham VH, Huan PV, Hoan BH, Nguyen DH, et al. A novel upconversion emission material based on Er^{3+}–Yb^{3+}–Mo^{6+} tridoped hydroxyapatite/tricalcium phosphate (HA/β-TCP). Journal of Alloys and Compounds. 2020;**827**:154288

[52] Milojkov DV, Silvestre OF, Vojislav Dj S, Janjić GV, Mutavdžić DR, Milanović M, et al. Fabrication and characterization of luminescent Pr^{3+} doped fluorapatite nanocrystals as bioimaging contrast agents. Journal of Luminescence. 2020;**217**:116757

[53] Zhou R, Li Y, Xiao D, Li T, Zhang T, Fub W, et al. Hyaluronan-directed fabrication of co-doped hydroxyapatite as a dual-modal probe for tumor-specific bioimaging. Journal of Materials Chemistry B. 2020;**8**:2107-2114

[54] Wang Y, Xue Y, Wang J, Zhu Y, Wang X, Zhang X, et al. Biocompatible and photoluminescent carbon dots/hydroxyapatite/PVA dual-network composite hydrogel scaffold and their properties. Journal of Polymer Research. 2019;**26**:248

[55] Xing Q, Zhang X, Wu D, Han Y, Wickramaratne MN, Dai H, et al. Ultrasound-assisted synthesis and characterization of heparin-coated Eu^{3+} doped hydroxyapatite luminescent nanoparticles. Journal of Colloid and Interface Science. 2019;**29**:17-25

[56] Machado TR, Leite IS, Inada NM, Li MS, da Silva JS, Andres J, et al. Designing biocompatible and multicolor fluorescent hydroxyapatite nanoparticles for cell-imaging applications. Materials Today Chemistry. 2020;**14**:100211

[57] Daneshvar H, Shafaei M, Manouchehri F, Kakaei S, Ziaie F. The role of La, Eu, Gd, and Dy lanthanides on thermoluminescence characteristics of nano-hydroxyapatite induced by gamma radiation. SN Applied Sciences. 2019;**1**:1146

[58] Barrera-Villatoro A, Boronat C, Rivera-Montalvo T, Correcher V,

Garcia-Guinea J, Zarate-Medina J. Cathodo- and thermally stimulated luminescence characterization of synthetic calcium phosphates. Spectroscopy Letters. 2018;**51**:22-26

[59] Huang P, Zhou B, Zheng Q, Tian Y, Wang M, Wang L, et al. Nano wave plates structuring and index matching in transparent hydroxyapatite-YAG:Ce composite ceramics for high luminous efficiency white light-emitting diodes. Advanced Materials. 2020;**32**:1905951

[60] Luo H, Xie J, Xiong L, Yang Z, Zuo G, Wang H, et al. Engineering photoluminescent and magnetic lamellar hydroxyapatite by facile one-step Se/Gd dual-doping. Journal of Materials Chemistry B. 2018;**6**:3515

[61] Pogosova MA, González LV. Influence of anion substitution on the crystal structure and color properties of copper-doped strontium hydroxyapatite. Ceramics International. 2018;**44**:20140-20147

[62] Al-Kattan A, Pascal D, Jeannette DG, Christophe D. Preparation and physicochemical characteristics of luminescent apatite-based colloids. Journal of Physical Chemistry C. 2010;**114**:2918-2924

[63] Zhang C, Li C, Huang S, Hou Z, Cheng Z, Yang P, et al. Self-activated luminescent and mesoporous strontium hydroxyapatite nanorods for drug delivery. Biomaterials. 2010;**31**:3374-3383

[64] Yang P, Quan Z, Li C, Kang X, Lian H, Lin J. Bioactive, luminescent and mesoporous europium-doped hydroxyapatite as a drug carrier. Biomaterials. 2008;**28**:4341-4347

[65] Bohner M. Calcium orthophosphates in medicine: From ceramics to calcium phosphate cements. Injury. 2000;**31**:37-47

[66] Constantz BR, Ison IC, Fulmer MT, Poser RD, Smith ST, Wagoner MV, et al. Skeletal repair by in situ formation of the mineral phase of bone. Science. 1995;**267**:1796-1799

[67] Benard J. Combinaisons avec le phosphore. In: Benard E, Bouissieres G, Brusset H, et al., editors. Nouveau trait6 de chimieminerale. Vol. 4. Paris: Masson; 1958. pp. 455-488

[68] Costantino PD, Friedman CD, Jones K, Chow LC, Pelzer HJ, Sisson GA Sr. Hydroxyapatite cement. I. Basic chemistry and histologic properties. Archives of Otolaryngology – Head & Neck Surgery. 1991;**117**:379-384

[69] Friedman CD, Costantino PD, Jones K, Chow LC, Pelzer HJ, Sisson GA. Hydroxyapatite cement. II. Obliteration and reconstruction of the cat frontal sinus. Archives of Otolaryngology – Head & Neck Surgery. 1991;**117**:385-389

[70] Khairoun I, Driessens FC, Boltong MG, Planell JA, Wenz R. Addition of cohesion promotors to calcium phosphate cements. Biomaterials. 1999;**20**:393-398

[71] Ciesla K, Rudnicki R. Synthesis and transformation of tetracalcium phosphate in solid state. Part I. Synthesis of roentgenographically pure tetracalcium phosphate from calcium dibasic phosphate and calcite. Polish Journal of Chemistry. 1987;**61**:719-727

[72] Kaygili O, Dorozhkin SV, Ates T, Ghamdi AA, Yakuphanoglu F. Dielectric properties of Fe doped hydroxyapatite prepared by sol–gel method. Ceramics International. 2014;**40**:9395-9402

[73] Ryaby JT. Clinical effects of electromagnetic and electric fields on fracture healing. Clinical Orthopaedics. 1998;**355**:S205-S215

[74] Scott G, King JB. A prospective, double-blind trial of electrical

capacitive coupling in the treatment of nonunion of long bones. The Journal of Bone and Joint Surgery. American Volume. 1994;**76A**:820-826

[75] Oishi M, Onesti ST. Electrical bone graft stimulation for spinal fusion: A review. Neurosurgery. 2000;**47**:1041-1055

[76] Goodwin CB, Brighton CT, Guyer RD, Johnson JR, Light KI, Yuan HA. A double-blind study of capacitively coupled electrical stimulation as an adjunct to lumbar spinal fusions. Spine (Phila Pa 1976). 1999;**24**:1349-1357

[77] Otter MW, McLeod KJ, Rubin CT. Effects of electromagnetic fields in experimental fracture repair. Clinical Orthopaedics and Related Research. 1998;**355**:S90-S104

[78] Marino AA, Becker RO, Bachman CH. Dielectric determination of bound water of bone. Physics in Medicine and Biology. 1967;**12**:367-378

[79] Lakes RS, Harper RA, Katz JL. Dielectric relaxation in cortical bone. Journal of Applied Physics. 1977;**48**:808-811

[80] Kaygili O, Keser S, Ates T, Ghamdi AA, Yakuphanoglu F. Controlling of dielectrical and optical properties of hydroxyapatite based bioceramics by Cd content. Powder Technology. 2013;**245**:1-6

[81] Iqbal N, Kadir MRA, Malek NANN, Mahmood NHB, Murali MR, Kamarul T. Characterization and antibacterial properties of stable silver substituted hydroxyapatite nanoparticles synthesized through surfactant assisted microwave process. Materials Research. 2013;**48**:3172-3177

[82] Horiuchi N, Endo J, Nozaki K, Nakamura M, Nagai A, Katayama K, et al. Dielectric evaluation of fluorine substituted hydroxyapatite. Journal of the Ceramic Society of Japan. 2013;**121**:770-774

[83] Shkir M, Kilany M, YahiaI S. Facile microwave-assisted synthesis of tungsten-doped hydroxyapatite nanorods: A systematic structural, morphological, dielectric, radiation and microbial activity studies. Ceramics International. 2017;**43**:14923-14931

[84] Thanigairul K, Elayaraja K, Magudapathy P, Mudali UK, Nair KGM, Sudarshan M, et al. Surface modification of nanocrystalline calcium phosphate bioceramic by low energy nitrogen ion implantation. Ceramics International. 2013;**39**:3027-3034

[85] ShKalil M, Beheri HH, Fattah WIA. Structural and electrical properties of zirconia/hydroxyapatite porous composites. Ceramics International. 2002;**28**:451-458

[86] Jonscher AK. The 'universal' dielectric response. Nature. 1977;**267**:673-679

[87] Dyre JC, Schrøder TB. Universality of ac conduction in disordered solids. Reviews of Modern Physics. 2000;**72**:873-892

[88] Yahia IS, Shkir M, AlFaify S, Ganesh V, Zahran HY, Kilany M. Facile microwave-assisted synthesis of Te-doped hydroxyapatite nanorods and nanosheets and their characterizations for bone cement applications. Materials Science and Engineering C. 2017;**72**:472-480

[89] Holzmann D, Holzinger D, Hesser G, Schmidt T, Knor G. Hydroxyapatite nanoparticles as novel low-refractive index additives for the long-term UV-photoprotection of transparent composite materials. Journal of Materials Chemistry. 2009;**19**:8102-8106

[90] Kotobuki N, Ioku K, Kawagoe D, Fujimori H, Goto S, Ohgushi H. Observation of osteogenic differentiation cascade of living mesenchymal stem cells on transparent hydroxyapatite ceramics. Biomaterials. 2005;**26**:779-785

[91] Eriksson M, Liu Y, Hu J, Gao L, Nygren M, Shen Z. Transparent hydroxyapatite ceramics with nanograin structure prepared by high pressure spark plasma sintering at the minimized sintering temperature. Journal of the European Ceramic Society. 2011;**31**:1533-1540

[92] Calderin L, Stott M, Rubio A. Electronic and crystallographic structure of apatites. Physical Review B. 2003;**67**:134106

[93] Rulis P, Ouyang L, Ching WY. Electronic structure and bonding in calcium apatite crystals: Hydroxyapatite, fluorapatite, chlorapatite, and bromapatite. Physical Review B. 2004;**70**:155104

[94] Slepko A, Demkov AA. First-principles study of the biomineral hydroxyapatite. Physical Review B. 2011;**84**:134108

[95] Wiglusz RJ, Bednarkiewicz A, Strek W. Synthesis and optical properties of Eu^{3+} ion doped nanocrystalline hydroxyapatites embedded in PMMA matrix. Journal of Rare Earths. 2011;**29**:1111-1116

[96] Mahraz ZAS, Sahar MR, Ghoshal SK, Dousti MR. Concentration dependent luminescence quenching of Er^{3+}-doped zinc boro-tellurite glass. Journal of Luminescence. 2013;**144**:139-145

[97] Pan A, Yang Z, Zheng H, Liu F, Zhu Y, Su X, et al. Changeable position of SPR peak of Ag nanoparticles embedded in mesoporous SiO_2 glass by annealing treatment. Applied Surface Science. 2003;**205**:323-328

[98] Apurba D, Kumar AC, Bharti GP, Behera RR, Mamilla RS, Khare A, et al. Effect of thickness on optical and microwave dielectric properties of hydroxyapatite films deposited by RF magnetron sputtering. Journal of Alloys and Compounds. 2018;**739**:729-736

[99] Matsunaga K, Kuwabara A. First-principles study of vacancy formation in hydroxyapatite. Physical Review B. 2007;**75**:014102

[100] Flores YJ, Quezada MS, Trigos JBR, Rojas LL, Suarez V, Mantilla A. Characterization of Tb-doped hydroxyapatite for biomedical applications: Optical properties and energy band gap determination. Journal of Materials Science. 2017;**52**:9990-10000

[101] Ma MY, Zhu YJ, Li L, Cao SW. Nanostructured porous hollow ellipsoidal capsules of hydroxyapatite and calcium silicate: Preparation and application in drug delivery. Journal of Materials Chemistry. 2008;**18**:2722-2727

[102] Zhanglei N, Zhidong C, Wenjun LI, Changyan S, Jinghua Z, Yang L. Solvothermal synthesis and optical performance of one-dimensional strontium hydroxyapatite nanorod. Chinese Journal of Chemical Engineering. 2012;**20**:89-94

[103] Zhang CM, Yang J, Quan ZW, Yang PP, Li CX, Hou ZY, et al. Hydroxyapatite nano- and microcrystals with multiform morphologies: Controllable synthesis and luminescence properties. Crystal Growth & Design. 2009;**9**:2725-2733

[104] Ling L, Yukan L, Jinhui T, Ming Z, Haihua P, Xu X, et al. Surface modification of hydroxyapatite nanocrystallite by a small amount of terbium provides a biocompatible fluorescent probe. Journal of Physical Chemistry C. 2008;**112**:1229-12224

[105] Han Y, Wang X, Li S, Ma X. Synthesis of terbium doped calcium phosphate nanocrystalline powders by citric acid sol–gel combustion method. Journal of Sol-Gel Science and Technology. 2009;**49**:125-129

[106] Arul KT, Ramya JR, Vanithakumari SC, Magudapathy P, Mudali UK, Nair KGM, et al. Novel ultraviolet emitting low energy nitrogen ion implanted magnesium ion incorporated nanocrystalline calcium phosphate. Materials Letters. 2015;**153**:182-185

[107] Arul KT, Ramya JR, Karthikeyan KR, Kalkura SN. A novel and rapid route to synthesize polyvinylalcohol/calcium phosphate nanocomposite coatings by microwave assisted deposition. Materials Letters. 2014;**135**:191-194

[108] Karthikeyan KR, Arul KT, Ramya JR, Nabhiraj PY, Menon R, Krishna JBM, et al. Core/shell structures on argon ions implanted polymer based zinc ions incorporated HAp nanocomposite coatings. Materials Science in Semiconductor Processing. 2019;**104**:104687

[109] Baskar S, Ramya JR, Arul KT, Nivethaa EAK, Mahadevan Pillai VP, Kalkura SN. Impact of magnetic field on the mineralization of iron doped calcium phosphates. Materials Chemistry and Physics 2018;**218**:166-171